ACS NANO

www.acsnano.org

ARTICLE

Emergent Cavity Junction around Metal-on-Graphene Contacts

Yuhao Zhao,[¶] Maëlle Kapfer,[¶] Megan Eisele, Kenji Watanabe, Takashi Taniguchi, Oded Zilberberg,* and Bjarke S. Jessen*

Cite This: *ACS Nano* 2025, 19, 18156–18163

Read Online

ACCESS | Metrics & More | Article Recommendations | Supporting Information

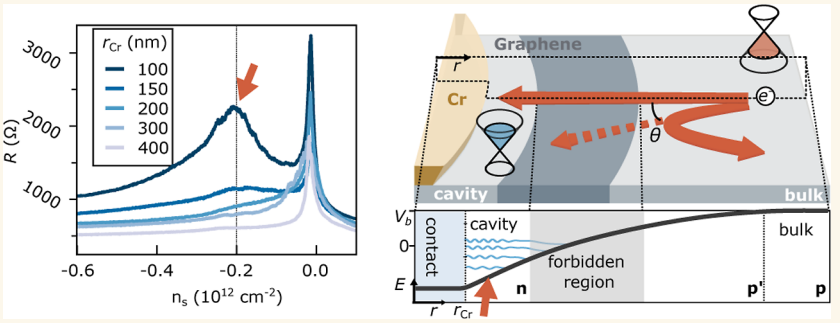

ABSTRACT: **Harnessing graphene's electronic properties for practical applications requires a comprehensive understanding of its interfaces with metal contacts, which are essential for device integration. Traditionally, the metal−graphene (MG) interface has been considered straightforward, primarily affecting graphene's work function through doping mechanisms. However, as device dimensions shrink to the sub-micrometer scale, subtle interfacial phenomena become increasingly significant. Here, we investigate transport phenomena occurring at high-quality, sub-micrometer metal contacts on graphene. Through transport measurements, electrostatic simulations, and first-principles calculations, we demonstrate that the metal contact induces a localized n-doped radial cavity, defined cooperatively by the metal-induced electrostatic potential and Klein tunneling. This mechanism leads to quantized energy states and secondary resistance peaks as a function of graphene doping that decrease with increasing contact size. In the presence of a perpendicular magnetic field, the cavity hosts a distinct set of Landau levels, resulting in the formation of a secondary bulk interacting with the intrinsic graphene bulk. This interplay enables the direct observation of topological edge states arising from bulk-boundary correspondence. Our results provide an improved understanding of metal−graphene interfaces, highlighting fundamental properties of graphene relevant for graphene-based nanoelectronic devices.**

KEYWORDS: *graphene, metal contacts, cavity states, Klein tunneling, Landau levels, quantum transport, electrostatic doping*

INTRODUCTION

Since the isolation of monolayer graphene, its exceptional electronic properties—such as high carrier mobility and tunable conductivity—have made it a promising candidate for next-generation nanoelectronic devices, including transistors, sensors, and spintronic components. A fundamental challenge in leveraging graphene's full potential lies in understanding and optimizing its interfaces with metal contacts, essential for integrating graphene into practical applications. Traditionally, the metal−graphene (MG) interface is understood using a relatively simple modification of graphene's work function alongside electrostatic considerations:[1−3] the potential of the graphene under the metal is pinned to the work function of the metal, and it gradually returns to the intrinsic graphene level away from the MG interface. This results in a doping gradient and the formation of pn and pp junctions, explaining characteristic asymmetries in two-terminal resistance measurements.[4,5]

However, as device dimensions shrink to the sub-micrometer scale, subtle interfacial phenomena become increasingly significant, necessitating a deeper investigation into the MG

Received: November 12, 2024
Revised: April 15, 2025
Accepted: April 16, 2025
Published: May 6, 2025

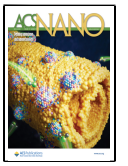

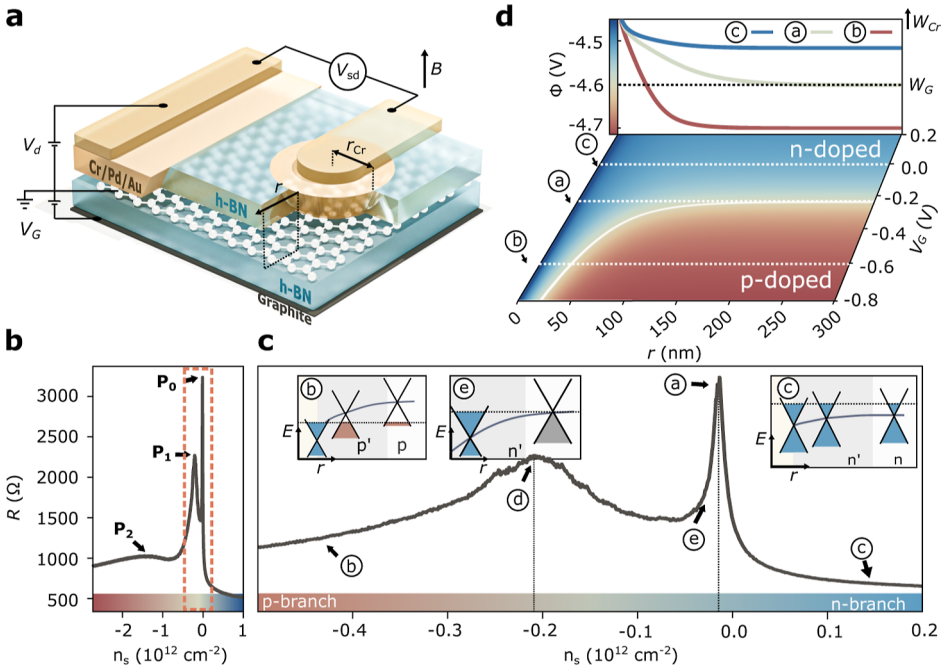

Figure 1. Emergent pn-junction at a metal−graphene interface. (a) Graphene is encapsulated in *h*BN and placed on a graphite back gate. Top contacts (Cr/Pd/Au) are gently deposited directly on the graphene after selectively etching through the top *h*BN layer. (b) Two-terminal resistance between the large contact (left) and a small dot contact (right) as a function of the carrier density n_s. We observe three resistance peaks P_0−P_2. (c) Zoom in on the dashed box in (b): ⓐ−ⓔ mark significant features, discussed in the text. (insets) Corresponding radial interpolation of the work function of graphene from the contact to the bulk. (d) The electrostatic potential around the contact is simulated using a finite-element method, see Methods. The obtained potential is plotted as a function of the carrier density, $n_s \propto V_G$, and the radial distance, r, starting from the contact edge. Presented linecuts at ⓐ−ⓒ mark scenarios where the pristine graphene is at the neutral point (white), p-doped (red), and n-doped (blue), respectively.

interface at the nanoscale. Other features often emerge in measurements, such as extra resistance peaks, which are considered unavoidable imperfections and are largely ignored as they are absent in four-terminal measurements.[6] Furthermore, such extra resistance features are often attributed to the graphene directly under the metal contacts.[7,8]

Here, we present findings that challenge this conventional understanding, revealing an unexpected and rich structure within the MG interface, which becomes particularly visible when examining contacts with sub-micrometer dimensions. To demonstrate this, we perform experiments in the simplest possible setup: a single high-quality metal contact on graphene connected to a larger reservoir contact. Using a combination of magnetotransport measurements, electrostatic simulations, and first-principles calculations, we uncover that the metal contact induces a localized n-doped cavity around itself due to an intricate electrostatic potential landscape shaped by the contact and the phenomenon of Klein tunneling. This cavity formation leads to quantized energy states and secondary resistance peaks in transport measurements, decreasing with increasing contact size.

Moreover, when a perpendicular magnetic field is applied, the system exhibits the formation of an emergent "second bulk" around the contact, characterized by a distinct set of Landau levels that interfere with those from the intrinsic graphene bulk. This interplay allows for the direct observation of topological edge states forming at the interface between the two bulks, providing further insights into the fundamental properties of graphene and the bulk-boundary correspondence in condensed matter physics. Our results underscore the critical need for precise knowledge of sub-micrometer graphene interfaces—a cornerstone for scaling down electronic components toward spintronics[9] and electron optics applications.[10,11] This understanding is particularly important as new generations of ever-improving two-dimensional material platforms unravel richer physics.[12−15]

RESULTS AND DISCUSSION

Transport Measurements. Our samples consist of monolayer graphene encapsulated within *h*BN supported by a graphite back gate, allowing modulation of the carrier density in the graphene layer, see Figure 1a. A fluorine-based dry etch (see Methods) is used to selectively etch the *h*BN to define top contacts. A metal stack of Cr/Pd/Au is then deposited on the exposed graphene resulting in a gentle defluorination process, such that a high-quality physisorbed metallic layer is formed directly on the graphene.[16−18] Source contacts are circular dots with a radius, r_{Cr}, down to 100 nm, while drain contacts are relatively large rectangles with areas exceeding 10 μm^2, allowing us to focus on the behavior of individual contacts. Due to the etch-angle of *h*BN, a frustum-shaped top contact is realized, where the radius of the top surface is slightly larger than that of the bottom surface (see Methods). We note that the distance between contacts eliminates unwanted coherence between source and drain contacts (see Supporting Information for experimental and numerical results for sub-micrometer contact distance).

We first measure the two-terminal resistance, R, as a function of the carrier density, n_s, by varying the back-gate voltage bias V_G, see Figure 1b. Unless otherwise stated, measurements were performed at a temperature of 10 mK, but we note that the phenomena we observe are relatively

https://doi.org/10.1021/acsnano.4c16191
ACS Nano 2025, 19, 18156−18163

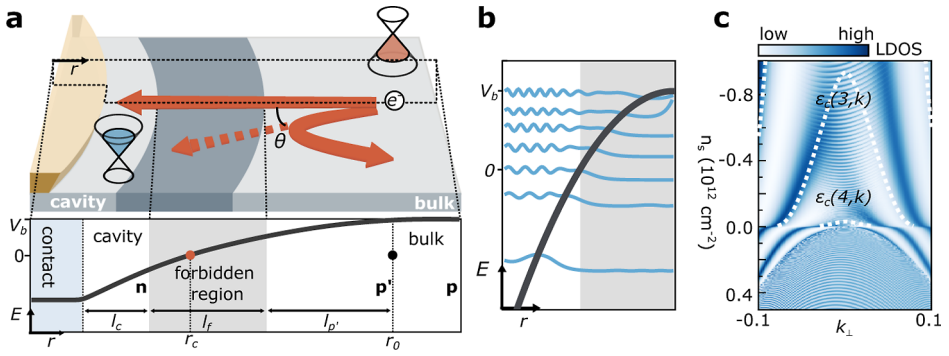

Figure 2. Doping-dependent cavity formation and energy quantization. (a) (upper panel) real space illustration of electron transport into the contact when the graphene bulk carrier density n_s is in the p-branch. Dopings are marked by the filling of the Dirac cone. Red arrows depict that Klein tunneling is relevant only at $k_\perp \approx 0$. (lower panel) Corresponding approximate parabolic function potential profile around the contact, see Figure 1d. The thick black line marks the position of the Dirac point along the radial direction. The interpolating on-site potential leads to the formation of three regions in the graphene (i) n-doped cavity (blue-filled cone) of width l_c, (ii) energetically forbidden region (dark gray) defining the pn-junction of width l_f, and (iii) the p-doped graphene bulk. The latter is split into two parts p′ and p, until the bulk doping is stabilized. (b) Sketch of bound states with discretized energy levels in the emergent cavity as a function of r. (c) Local density of states (LDOS) of the bound states (up to $r \approx 50$ nm) as a function of the transverse momentum $k_\perp$ and doping level n_s, see Methods. Fine oscillations are due to finite-size effects in the numerics. Modes around $k_\perp \approx 0$ penetrate the cavity due to Klein tunneling. The white dashed line marks the analytically obtained spectrum of the cavity mode $\epsilon_c(m, k_\perp)$, see Methods.

insensitive to temperature (see Supporting Information). We use bias voltages around 100 μV to avoid any unwanted charge-accumulation on the substrate.[19] Scanning over n_s from -3×10^{-12} to 1×10^{-12} cm^{-2}, we observe a sharp resistance peak $\mathbf{P}_0$ at $n_s = 0$ cm^{-2}, and two smooth resistance peaks $\mathbf{P}_1$ and $\mathbf{P}_2$ at $n_s = -0.2 \times 10^{-12}$ cm^{-2} and $n_s = -1.2 \times 10^{-12}$ cm^{-2}, respectively. Narrowing our focus to the n_s regime around $\mathbf{P}_0$, we attribute the sharp peak $\mathbf{P}_0$ to the Dirac point of the bulk graphene, marked by ⓐ in Figure 1c. As $|n_s|$ increases (marked by ⓔ), R rapidly drops due to the increasing density of states of the bulk graphene, DOS $\propto \sqrt{n_s}$. Asymptotically away from the first peak, R exhibits an asymmetric imbalance in the p- and n-doped bulk regions, dubbed p- and n-branch and marked by ⓑ and ⓒ, respectively. This is caused by the pinned potential under the metal contact, which effectively leads to the formation of a pn junction between the p-doped bulk graphene and an n-doped region around the contact; the asymmetry in R is then due to Klein tunneling filtering of conduction channels.[1,4,20] The appearance of a single secondary peak is conventionally attributed to the gap opening due to the g/hBN misalignment,[21,22] or to the pinned Dirac point of the graphene under the contact.[23] However, we observe that the soft peak $\mathbf{P}_1$ (marked by ⓓ) appears too close to the main peak $\mathbf{P}_0$, rendering the g/hBN misalignment explanation inapplicable. This, and the appearance of the additional smooth peak $\mathbf{P}_2$, points toward previously overlooked mechanisms, which go beyond standard graphene pn-junction physics.

Finite Element Simulation. To gain insight into the microscopic origin of these resistance features, we first calculate, using a finite-element simulation, the electrostatic potential profile of the graphene, Φ, around the metal contact, see Figure 1d and Methods. The convex edge of the contact suppresses interference effects and allows us to isolate the subtle physics within the contact/bulk region.[24] We employ boundary conditions fixed by the work function of chromium $W_{Cr} = 4.3$ V[23] and graphene $W_G = 4.6\,\mathrm{V} + \sqrt{\pi v_F^2 \hbar^2 C}\sqrt{V_G}$,[25−27] where v_F is the Fermi velocity; $\hbar$ is the reduced Planck constant and the geometric capacitance $C = 2.72 \times 10^{15}$ V^{-1} cm^{-2}. Under the contact we assume that the potential of the graphene is pinned to W_{Cr} regardless of V_G,[3,23] i.e., the graphene is n-doped there. Radially away from the contact edge, the electrostatic potential continuously transitions from the pinned value to the work function of the bulk graphene, set by V_G. In the p-branch, a pn-junction emerges ∼30−150 nm away from the contact's edge, marked by a solid white line in Figure 1d. The emergence of a pn-junction as a function of V_G is in agreement with the asymmetry in resistance observed in Figure 1c. Moreover, to verify the obtained distance between the pn-junction and the contact's edge, which is seemingly shorter compared with previous research,[28,29] we perform the same measurement (see Figure S6) with two contacts that are distanced 350 nm from each other. We observe the asymmetry in resistance, suggesting the existence of a very narrow pn-junction close to the contact's edge.

Cavity Forming around the Contact. For $n_s < -0.1 \times 10^{-12}$ cm^{-2}, the n-doped region between the contact's edge and the charge neutrality point (CNP) can become very narrow with a radial width down to ∼30 nm, see Figure 1d. To explore the prospective quantization of modes in this narrow region, we write the graphene Hamiltonian around the contact using a mixed position and momentum representation, i.e., using a finite radial extent $\hat{r}$ and transverse momentum $k_\perp \equiv |\mathbf{k}| \sin(\theta)$, where θ is the incident angle at the interface, and $\mathbf{k}$ is the 2D momentum, see Figure 2a. We introduce the interpolating electrostatic potential as an inverse-parabola on-site term $V(r, V_b)$, characterized by two parameters $V_0 = V(0, V_b)$ and $\alpha = \partial_r^2 V$ (see Methods). This on-site term extends between the contact and the graphene bulk dopings, while the latter is denoted by V_b, and experimentally tuned by V_G. It engenders a quasi-triangular radial cavity around the contact with bound modes, see Figure 2b. The cavity width is $k_\perp$-dependent: consider a state propagating outward from the contact along $\hat{r}$; it backscatters when the on-site energy is equal to the kinetic energy in the transverse direction, i.e., we have a classical turning point when $|V_b| = v_F|k_\perp|$. Similarly, another classical turning point manifests for an inbound electron propagating toward the contact. The resulting two classical turning points thus determine an effective $k_\perp$-dependent (i) width for the cavity $l_c = \sqrt{|V_b - V_0|/\alpha} - \sqrt{(V_b + |k_\perp| v_F)/\alpha}$,

https://doi.org/10.1021/acsnano.4c16191
ACS Nano 2025, 19, 18156−18163

as well as, (ii) a classically forbidden region of width l_f between the two turning points, see lower panel of Figure 2a. We observe that both l_c and l_f decrease with increasing n_s. The former entails that the energy spacing between the cavity levels increases with n_s. The latter implies that the tunneling barrier into the bulk becomes narrower with increasing n_s. We verify this prediction using a Green's function method, by which we numerically obtain the local density of states (LDOS) spectrum in the cavity, see Figure 2b,c. Crucially, we observe a discrete set of energy levels that depend on $k_\perp$ alongside contributions from Klein tunneling at $k_\perp \approx 0$. An analytically obtained spectrum $\epsilon_c(m, k_\perp)$ (see Methods) fits well with the result. In the n-branch, the absence of a forbidden region allows states near the contact to strongly hybridize with the n-doped graphene bulk, leading to a continuous dispersion.

We move to calculate the conductance $G_{k_\perp}$ between the contact and the bulk (see Figure 3a)

$$G_{k_\perp}(V_b) \propto |t_{pn}(V_b, k_\perp)|^2 \rho_{k_\perp}(V_b) \quad (1)$$

where t_{pn} is the tunneling amplitude through the forbidden region and $\rho_{k_\perp}(V_b)$ is a $k_\perp$-dependent tunneling density of states; the latter depends on both the density of states in the bulk and in the cavity. We observe strikingly different behavior in the p- and n-branches. In the n-branch, where no pn-junction nor cavity form, $G_{k_\perp}$ exhibits a parabolic shape as a function of $k_\perp$ and n_s, indicating that transport is dominated by the density of states of the graphene bulk. In the p-branch, instead, $G_{k_\perp}$ is restricted to small $k_\perp$, due to filtering of t_{pn} via Klein tunneling through the forbidden region. Crucially, whenever the cavity modes coincide with the allowed transport window, the $G_{k_\perp}$ intensity increases, indicating a modification of the density of scattering states $\rho_{k_\perp}(V_b)$.

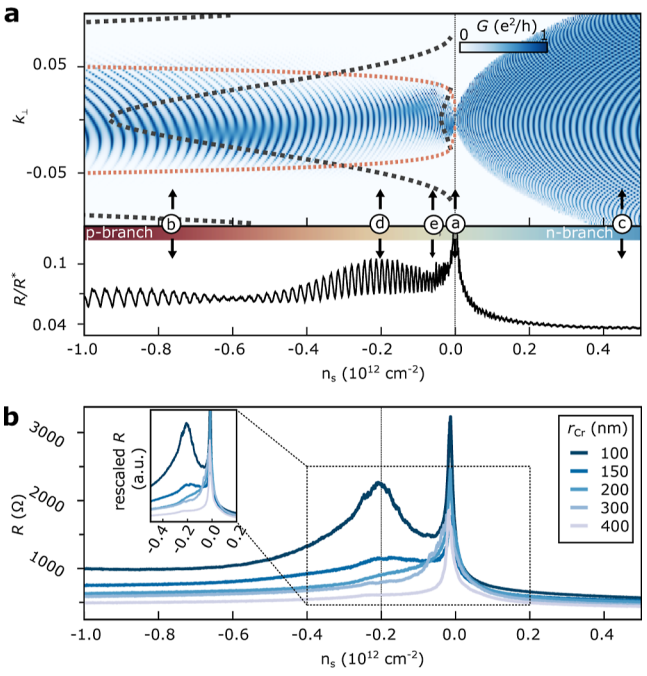

Figure 3. Cavity states modulated resistance and the impact of contact size. (a) (upper panel) Conductance [cf. eq 1] as a function of momentum $k_\perp$ and carrier density n_s. Fine oscillations are due to the finite size of the numerical solution. Red dashed lines encircle the regime of high-tunneling over the forbidden region where $t_{pn} > 0.5$, i.e., where Klein-tunneling is dominant (see Methods). The dispersion of the cavity modes $\epsilon_c(m, k_\perp)$ is marked by gray dashed lines, cf. Figure 2c. (lower panel) The corresponding resistance as a function of n_s in units of $R^* = h/(2e^2)$. A soft resistance peak around $n_s = -0.2 \times 10^{12}$ cm^{-2} appears with small oscillations due to finite-size numerical artifacts. (b) Experimentally measured resistance as a function of the carrier density n_s for different dot contacts with radii ranging from 100 to 400 nm. (inset) Zoom-in plot of R in the marked area in (a). The resistance is rescaled relative to the R measured with $r_{Cr} = 100$ nm at $n_s = 1.0 \times 10^{12}$ cm^{-2}.

The total resistance is obtained as $R = [\sum_{k\perp} G(k_\perp)]^{-1}$, see bottom panel of Figure 3a, which we compare with Figure 1c. Starting from the neutral point ⓐ, the resistance is high due to the absence of states in the bulk. As n_s increases toward ⓒ in the n-branch, the resistance drops due to the increasing DOS in the bulk. Conversely, as n_s decreases toward ⓔ, the resistance initially decreases as a dense spectrum of cavity states is available at small $k_\perp$. The $\mathbf{P}_1$ peak at $n_s \approx -0.2 \times 10^{12}$ cm^{-2}, marked as ⓓ, appears when the cavity modes are off-resonant with the Klein-tunneling allowed transport channels. Finally, at ⓑ, although the cavity states found at small $k_\perp$ can assist the tunneling to the contact, their impact is less pronounced as the narrow cavity and forbidden region allow for direct cotunneling between the bulk and the contact. Nevertheless, when n_s continues to decrease toward the deeply p-doped regime (see Figure S4), a second smooth peak is observed where the cavity modes are once more off-resonant with the allowed transport channels, thus, yielding a similar feature as $\mathbf{P}_2$.

Scaling with Contact Size. Our effective cavity model suggests that the secondary peak originates from the reduced DOS in the emergent confined cavity around the contact, and not from the graphene directly under the metal. As such, by increasing the contact size, we expect an increase in the DOS due to added transverse momentum modes, and hence a reduction in the peak's height. To probe our prediction, we repeat the two-terminal resistance measurement using dot contacts with radii r_{Cr} ranging from 100 to 400 nm, see Figure 3b. As the size of the metal contact increases, more transport channels participate, and the overall R is reduced. Nonetheless, the peak is observed for all contact sizes at the same carrier density $n_s \approx -0.2 \times 10^{12}$ cm^{-2}, showing that the secondary resistance peak indeed depends only on the potential environment created by the metal contact. To better isolate the peak's qualitative R reduction from the increased cavity DOS on top of the R reduction due to the contact size and contact resistance, we rescale all measured plots relative to the R in the n-region, where no cavity forms, see inset of Figure 3b. The cavity remains visible while showing a clear reduction with the cavity diameter.

Dual Landau Fans. Subjecting the MG system to a perpendicular magnetic field reveals further intricate details about its electronic properties. In Figure 4a, we present the measured differential resistance $(\delta R/\delta V_G)$ as a function of the magnetic field, B, and carrier density, n_s. While an expected Landau fan (LF) pattern emerges out of graphene's CNP, interestingly, a second LF appears near $n_s \approx -0.24 \times 10^{12}$ cm^{-2}, i.e., coinciding closely with the first cavity-induced resistance peak, $\mathbf{P}_1$. Probing a larger density range (Figure 4b), apparent phase slips at the intersections of the two LFs are evident. While the primary LF is associated with the bulk graphene, the origin of the second LF is unconventional: (i)

https://doi.org/10.1021/acsnano.4c16191
ACS Nano 2025, 19, 18156−18163

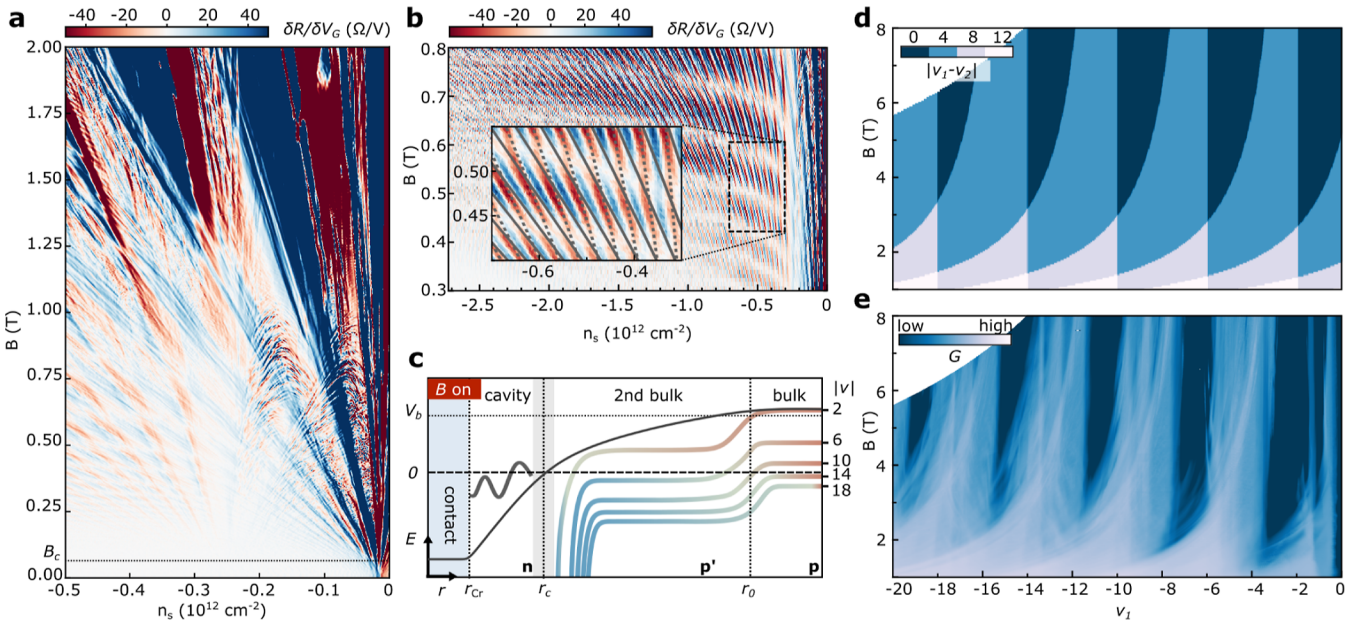

Figure 4. Formation of a second bulk with a perpendicular magnetic field. (a) Differential resistance at low-field and small n_s with the radius of the dot contact r_{Cr} = 200 nm. Two distinct sets of Landau Fans are observed. (b) Differential resistance for higher density values with inset highlighting phase slips at the crossing of the Landau levels. (c) Sketch of "wedding cake" potential profile around the contact forming under a perpendicular magnetic field. The smooth interpolating potential (black solid line) is renormalized and Landau levels appear along a step-like energy profile (colored lines), cf. ref 30. (d) The difference between the fillings of the two bulks $|\nu_1 - \nu_2|$, as a function of the filling factor of the graphene bulk ν_1 and the magnetic field. (e) The longitudinal conductance G measured as a function of ν_1 and B. The conductance exhibits a triangular-shaped pattern resembling the $|\nu_1 - \nu_2|$ from (d). We observe further splitting between the Landau fans of the secondary bulk.

we cannot attribute it to the recoil band forming from the misalignment between graphene and *h*BN,[21,22] as the observed $n_s \approx -0.24 \times 10^{12}$ cm^{-2} is too small compared with the typical case related to such recoil; additionally, $\mathbf{P}_1$ and the source of the emanating secondary LF occurs at a similar value of n_s across all our MG samples, regardless of g/*h*BN alignment (not shown); (ii) the second LF manifests only beyond a finite field strength ($B_c \approx 0.1$ T), which may hint toward a Fock−Darwin cascade of states within the emergent cavity;[31] we rule out this explanation as the cavity length ($l_c \approx 20$ nm) is smaller than the magnetic length ($l_{B_c} \approx 80$ nm).

Direct View of the Bulk-Boundary Correspondence. We attribute the second LF to a secondary bulk forming between the cavity and the bulk graphene. Without a magnetic field, a smoothly interpolating p′-doped region exists between the bulk and the cavity (p′ ≠ p), cf. Figure 3a. When the magnetic field is applied, electrons can be trapped in the p′-doped region if their cyclotron movement is confined within the region's scale, i.e., when $l_{B_c} \approx l_{p'}$.[32] Similar to LLs, these electrons fall into highly degenerate energy levels, where Coulomb interaction can renormalize the potential profile.[30] Consequently, the potential in the p′-doped region flattens out such that a second bulk effectively forms and the overall potential exhibits steps akin to a "wedding cake", see Figure 4c. The energetic offset at the emergent bulk implies a secondary LF emanating from a carrier density n_s, where the graphene bulk is p-doped, i.e., at $n_s < 0$ cm^{-2}. Furthermore, this offset implies that the Landau level filling factors, $\nu = 4(n + 1/2)$, differ between two bulks. We are hence in a scenario where the quantum Hall effect's Chern numbers $n \in \mathbb{N}$ vary radially away from the MG contact between the two differently doped bulks. Due to the different topology between the two bulks, at the interface between them ($r \sim r_0$), $|\nu_1 - \nu_2|$ edge modes appear,[33] where $\nu_{1,2}$ are the filling factors in the main and the secondary bulks, respectively, see Figure 4d. In Figure 4c, we illustrate this bulk-boundary correspondence,[34] i.e., the continuous change in bulk filling leads to $|\nu_1 - \nu_2|$ intersections of LLs with the Fermi level ($E = 0$) at the interface between the two bulks ($r \sim r_0$), thus forming edge states. As the emergent edge states appear near the MG contact, we expect the conductance to be dominated by the presence of these transport channels. We confirm this model prediction by measuring within the same parameter range of Figure 4d, see Figure 4e. We observe a strong agreement between the measured conductance G and the residual filling $|\nu_1 - \nu_2|$. Furthermore, we observe splitting of the LLs that appear as a nested set of triangular shapes; we attribute these splittings to the lifting of the spin-valley degeneracy in the secondary bulk.

CONCLUSION

Our work reveals complexity in the seemingly simple system of a metal contact on graphene. Contrary to the conventional picture of mere doping, the contact creates an intricate potential landscape that gives rise to quantized cavity states. Under a magnetic field, this landscape further evolves, spawning a distinct emergent bulk with its own set of Landau levels. This second bulk, arising from the interplay between the metal-induced potential and electron−electron interactions, results in the formation of topological edge states at the interface between the two bulks. The appearance of these features—quantized cavity states, a secondary bulk, and edge states—within a single graphene sheet suggests that contact phenomena can involve additional complexity with implications for device physics. These effects may be relevant for future approaches to controlling transport properties in

https://doi.org/10.1021/acsnano.4c16191
ACS Nano 2025, 19, 18156−18163

graphene-based electronic devices. For instance, confined regions with distinct topological properties could be used in studies of topological electronics. In addition, the observation of edge states at boundaries between distinct doping regions provides a platform for examining the properties of topological transport in condensed matter systems.

METHODS

Device Fabrication. Graphene and *h*BN are exfoliated on a SiO_2/Si substrate, and single-layer graphene is automatically identified using its contrast relative to the substrate.[35] The graphene heterostructures are fabricated with a standard dry-stacking method[13,36,37] using a polycarbonate-coated polydimethylsiloxane stamp. We sequentially pick up and intentionally misalign *h*BN (∼30 nm), monolayer graphene, *h*BN (∼30 nm), and deposit these on a ∼5 nm thick graphite flake. Layers are picked up by raising our substrate temperature to about 110 °C during stamp contact, and dropped onto the graphite flake by melting the polycarbonate at around 190 °C. Subsequently, we use electron beam lithography to define contacts in a two-step process. First, the top *h*BN is gently etched using a highly selective fluorine-based dry etch, based on either CF_4 or SF_6, to expose the graphene. Crucially, this process does not etch through the graphene (Figure S1). This is directly followed by a metal deposition of Cr/Pd/Au (∼3/15/60 nm) to contact the graphene. A second lithography step is done to draw electrical leads to the patterned nanostructures. All metals are deposited at pressures of $\sim 10^{-8}$ Torr and rates of 0.3, 1, and 1 Å/s for Cr, Pd, and Au, respectively.

Measurements. Transport measurements were performed in a Bluefors dry dilution cryostat achieving a temperature at the mixing chamber of 10 mK. The electrical resistance was measured in a two-terminal configuration using Stanford Research SR860 lock-in amplifiers while sourcing 100 μV at a reference frequency of 17.777 Hz to efficiently reject noise. Commercial Q-Devil filters are placed on the mixing chamber of the cryostat adding a 5k Ω impedance in series with the device which we subtract in the presented data.

Finite Element Calculation. We conduct the COMSOL simulation using its semiconductor module, where we define a radially symmetric geometry to model the top contact and its surroundings, see Figure S2a. From bottom to top, we effectively introduce the combined effect of the graphite back-gate together with the separating *h*BN layer beneath the graphene by defining the bottom surface of the whole geometry as a Thin Insulator Gate. Thus, the back-gate voltage V_G can be applied to the system. To the bulk of the lowest layer, we assign a material *C* with electron affinity defined as 4.6 V in accordance with measured values of graphene.[25−27] The linear dispersion of graphene is introduced by defining the density of states in the valence and conduction bands as $n = V_G \times 2.72 \times 10^{12}$ m^{-2}.

The graphene layer is covered by two separate parts from the top. The metal contact is defined as the frustum-shaped area in the center with material type air and metal contact interface to the top surface of the graphene layer. For the latter, we use the work function of chromium $W_{Cr} = 4.3$ V.[23] The top peripheral area pertains to the *h*BN layer that encapsulates the graphene from the top. Its material is set as SiO_2, whereas the work function and the band gap are adjusted for *h*BN.

Effective Model for the Emergent Parabolic Potential. We model the interpolating electrostatic potential ϕ using a parabolic onsite function $V(r, V_b)$ on a tight-binding lattice, where the Fermi level $E = 0$ is defined with respect to the primitive work function of graphene. The onsite potential is a piece-wise function

$$V(r, V_b) = \begin{cases} V_0 & r < 0 \\ V_b + \mathrm{sign}(V_0 - V_b)\alpha(r - r_0)^2 & 0 \le r < r_0 \\ V_b & r \ge r_0, \end{cases} \tag{2}$$

where $V_0 = -0.35t$ and $r_0 = \sqrt{|V_b - V_0|/\alpha}$. The smoothness of V is defined as $\alpha = 0.000027t$/site (we omit the unit of α in the following discussion), such that the electrostatic potential obtained by COMSOL is best fitted around the cavity region, see Figure S2d. We define the hopping amplitude $t = 0.46$ eV to model a 500 nm system with 301 sites.

Quasi-2D Model. The tight-binding Hamiltonian of graphene system reads

$$H_{2D} = t\sum_{m,n} (c^\dagger_{A,m,n}c_{B,m,n} + c^\dagger_{B,m+1,n}c_{A,m,n} + c^\dagger_{B,m,n+1}c_{A,m,n} + c.\,c.\,) \tag{3}$$

where $c^\dagger_{l,m,n}$ denotes an electron creation operator on the sublattice $l = A(B)$ at site (m, n). Next, as the interface to the contact is a closed circle, we impose a cylindric geometry, i.e. the boundary in *n*-direction is closed with periodic boundary conditions such that we can reduce the 2D system to a collection of 1D channels labeled by the good quantum number $k_\perp$. The left end of the cylinder corresponds to the interface to the contact (Figure S3a). Moreover, we introduce the potential profile in eq 2 modeling the electrostatic potential along the $\hat{r}$ direction. The corresponding Hamiltonian is given as

$$H_{k_\perp} = t\sum_m (c^\dagger_{A,m,k_\perp}c_{B,m,k_\perp} + c^\dagger_{B,m+1,k_\perp}c_{A,m,k_\perp} + e^{i\sqrt{3}k_\perp}c^\dagger_{B,m,k_\perp}c_{A,m,k_\perp} + c.\,c.\,) + \sum_m \sum_{l=A,B} V(m, V_b)c^\dagger_{l,m,k_\perp}c_{l,m,k_\perp}, \tag{4}$$

where $m = 1, ..., M$ labels the site along *r*-direction. The spectrum is obtained using exact diagonalization as a function of $k_\perp$ with $V_b = 0$, see Figure S3b. We find that there are discrete spectrum flows existing next to the continuous spectrum. While the latter represents the continuous energy levels in the graphene bulk, the former indicates the existence of the discretized modes confined in the cavity.

Local Density of States and Conductance. We use the Green's function method with the 1D system in eq 4 to calculate the local density of states (LDOS) and the transport across the system. The local density of states at site m and at the Fermi surface $E = 0$ is given as[6]

$$\mathrm{LDOS}_{k_\perp}(m) = -\frac{1}{\pi}\mathrm{Im}[G^R_{k_\perp}(m, m; 0)] \tag{5}$$

where $G^R_{k_\perp}(m, m'; E)$ is the retarded Green's function between site m and m' at energy E. As the system is coupled to leads at the two ends, the retarded and advanced Green's functions are modified by the interaction between the system and leads as

$$\begin{aligned} G^R_{k_\perp}(m, m'; E) &= [E - H_{k_\perp} - \Sigma^R_l - \Sigma^R_r]^{-1}_{m,m'} \\ G^A_{k_\perp}(m, m'; E) &= [E - H_{k_\perp} - (\Sigma^R_l)^\dagger - (\Sigma^R_r)^\dagger]^{-1}_{m,m'} \end{aligned} \tag{6}$$

where $\Sigma^R_{l/r} = -0.4\exp(\sqrt{(E - V_0)})$ is the self-energy due to the leads. We calculate the LDOS for each site m as a function of V_b and $k_\perp$. To illustrate the discrete energy levels in the cavity, we average over its extent $\mathrm{DOS}_c = \sum_{m=1,\cdots 30}\mathrm{LDOS}(m)$, i.e. we sum over the LDOS of the first 30 sites (≈50 nm) next to the contact. See in Figure S3c.

Next, the $k_\perp$ conductance between the two leads is $G_{k\perp} = e^2T_{k_\perp}/h$, where the transmission probability $T_{k_\perp}$ is obtained as

$$T_{k_\perp} = \mathrm{Tr}[\Gamma_l G^R_{k_\perp}\Gamma_r G^A_{k_\perp}] \tag{7}$$

where $\Gamma_{l/r} = i[\Sigma^R_{l/r} - (\Sigma^R_{l/r})^\dagger]$. We numerically evaluate eq 7 as a function of $k_\perp$ and V_b, see Figure S3d. To compare with the experiments, we introduce the carrier density n_s using the relation $n_s = (V_b t)^2/(\pi v_F^2\hbar^2)$, where $v_F = 10^6$ m/s is the Fermi velocity of the graphene.

We note that due to the finite size of the sample in the numerics ($M = 801$ sites). The finite sampling of the longitudinal momentum leads to a finite energy spacing $\Delta E = hv_F/(aM) = 3.1$ meV of the

https://doi.org/10.1021/acsnano.4c16191
ACS Nano 2025, 19, 18156−18163

states in the bulk, where a = 1.67 nm is the spacing of the quasi-2D model in the numerics. Analogous to the mechanism of the resonance bump due to the cavity states, the discretized bulk states here yield finer oscillations with the period given by the energy spacing ΔE. In the experiments, this effect is not observed, as the sample size is much larger such that ΔE vanishes.

Analytic Expression for the Cavity Spectrum and Tunneling Strength t_{pn}. We calculate the spectrum of the cavity mode using the WKB approximation. For the mode with transverse momentum $k_\perp$ in a cavity of length l_c, we obtain the Sommerfeld quantization condition by requiring the continuity of the wave function at the boundary $r = l_c$[38]

$$\mathrm{Re}\left(2\int_0^{l_c} \mathrm{d}r \frac{1}{v_{\parallel}}\sqrt{[E - V(r, V_b)]^2 - v_\perp^2 |k_\perp|^2}\right) = \left(2m - \frac{1}{2}\right)\pi \tag{8}$$

where $m \in \mathbb{N}^+$ is an integer number characterizing the quantized energy levels. To cope with the 1D Hamiltonian in eq 4, we chose the Fermi velocity $v_\parallel = 1$ and $v_\perp = 3/2$ for the energy in the unit of t. To study the DOS inside the cavity, we solve V_b as a function of $k_\perp$ for $E = 0$ and $m \in \mathbb{N}^+$ using the equation above, i.e. for a mode confined in the cavity characterized by the momentum $k_\perp$, it can be found at the Fermi level ($E = 0$) when the graphene is doped to V_b. As such, we obtain an effective spectrum $\epsilon_c(m, k_\perp)$ for the cavity mode, where $\epsilon_c(m, k_\perp) \equiv V_b$ for given quantized number m and momentum $k_\perp$.

We numerically evaluate the integral in eq 8 and show the obtained $\epsilon_c(m, k_\perp)$ as the white dashed line in Figure S3c. The analytical results agree well with the LDOS obtained numerically.

Finally, we estimate the transmission amplitudes t_{pn} using the WKB approximation[24]

$$t_{pn} = \mathrm{e}^{-\mathrm{Im}\int_{l_c}^{l_c+l_f} k_\parallel(r)\mathrm{d}r} \tag{9}$$

where the imaginary wave-vector $k_\parallel = \sqrt{V_\alpha(r, V_b)^2 - v_F^2|k_\perp|^2}/v_F$ characterizes the exponentially decaying wave function in the classically forbidden region with a length $l_f = \sqrt{(V_b + v_F|k_\perp|)/\alpha} - \sqrt{(V_b - v_F|k_\perp|)/\alpha}$. In Figure S3e, we show t_{pn} obtained by numerically evaluating eq 9 as a function of the density carrier n_s and the momentum $k_\perp$.

ASSOCIATED CONTENT

Supporting Information

The Supporting Information is available free of charge at https://pubs.acs.org/doi/10.1021/acsnano.4c16191.

> Additional experimental data including temperature dependence measurements (10 mK−1.7 K) and transport simulations up to 5 K; finite-element electrostatic simulations and transport results for sub-micrometer contact separations; details on selective etching process; and numerical analysis of cavity states (PDF)

AUTHOR INFORMATION

Corresponding Authors

Oded Zilberberg − *Department of Physics, University of Konstanz, Konstanz 78464, Germany*; Email: oded.zilberberg@uni-konstanz.de

Bjarke S. Jessen − *Department of Physics, Technical University of Denmark, Kongens Lyngby 2800, Denmark; Department of Physics, Columbia University, New York, New York 10027, United States*; orcid.org/0000-0001-8453-6125; Email: bsoje@dtu.dk

Authors

Yuhao Zhao − *Institute for Theoretical Physics, ETH Zurich, Zurich 8093, Switzerland*

Maëlle Kapfer − *Department of Physics, Columbia University, New York, New York 10027, United States*

Megan Eisele − *Department of Physics, Columbia University, New York, New York 10027, United States*

Kenji Watanabe − *Research Center for Electronic and Optical Materials, National Institute for Materials Science, Tsukuba 305-0044, Japan*; orcid.org/0000-0003-3701-8119

Takashi Taniguchi − *Research Center for Materials Nanoarchitectonics, National Institute for Materials Science, Tsukuba 305-0044, Japan*; orcid.org/0000-0002-1467-3105

Complete contact information is available at: https://pubs.acs.org/10.1021/acsnano.4c16191

Author Contributions

¶Y.Z. and M.K. contributed equally to this work. B.S.J. and M.K. prepared the samples and performed the transport measurements. Y.Z. performed finite element simulations, cavity simulations, and developed the analytical model. O.Z. developed the analytical model and provided technical support for the numeric simulations. B.S.J., M.K., and Y.Z. analyzed the data. K.W. and T.T. grew and provided the *h*BN crystals. Y.Z., B.S.J., M.K., and O.Z. wrote the paper with input from all authors.

Notes

The authors declare no competing financial interest.

This work was previously posted as a preprint: Zhao, Y.; Kapfer, M.; Watanabe, K.; Taniguchi, T.; Zilberberg, O.; Jessen, B. S. Emergent Cavity Junction around Metal-on-Graphene Contacts. 2024, arXiv:2408.10973. arXiv. 10.48550/arXiv.2408.10973 (accessed March 28, 2025).

ACKNOWLEDGMENTS

O.Z. and Y.Z. acknowledge support by the Swiss National Science Foundation, the Deutsche Forschungsgemeinschaft (DFG) through Project no. 449653034, and Eidgenössische Technische Hochschule Zürich research Grant no. ETH-28 23-1. B.S.J. and M.K. acknowledge support from the Center for Programmable Quantum Materials (Pro-QM), an Energy Frontier Research Center funded by the US Department of Energy (DOE), Office of Science, Basic Energy Sciences (BES), under award DE-SC0019443. K.W. and T.T. acknowledge support from the JSPS KAKENHI (Grant Numbers 21H05233 and 23H02052), the CREST (JPMJCR24A5), JST and World Premier International Research Center Initiative (WPI), MEXT, Japan. B.S.J. gratefully acknowledges support from the Villum Foundation and Novo Nordisk Foundation grant NNF23OC0084494 (BioNwire). We thank Peter Bøggild and Cory R. Dean for useful discussions and feedback on the manuscript.

REFERENCES

(1) Huard, B.; Stander, N.; Sulpizio, J. A.; Goldhaber-Gordon, D. Evidence of the role of contacts on the observed electron-hole asymmetry in graphene. *Phys. Rev. B* **2008**, *78*, 121402.

(2) Allain, A.; Kang, J.; Banerjee, K.; Kis, A. Electrical contacts to two-dimensional semiconductors. *Nat. Mater.* **2015**, *14*, 1195−1205.

(3) *Frontiers of Graphene and Carbon Nanotubes: Devices and Applications*; Matsumoto, K., Ed.; Springer Japan: Tokyo, 2015.

(4) Xia, F.; Perebeinos, V.; Lin, Y.-m.; Wu, Y.; Avouris, P. The origins and limits of metal−graphene junction resistance. *Nat. Nanotechnol.* **2011**, *6*, 179−184.
(5) Bartolomeo, A. D.; Giubileo, F.; Romeo, F.; Sabatino, P.; Carapella, G.; Iemmo, L.; Schroeder, T.; Lupina, G. Graphene field effect transistors with niobium contacts and asymmetric transfer characteristics. *Nanotechnology* **2015**, *26*, 475202.
(6) Datta, S. *Electronic Transport in Mesoscopic Systems Cambridge Studies in Semiconductor Physics and Microelectronic Engineering*; Cambridge University Press, 1995.
(7) Bartolomeo, A. D.; Giubileo, F.; Santandrea, S.; Romeo, F.; Citro, R.; Schroeder, T.; Lupina, G. Charge transfer and partial pinning at the contacts as the origin of a double dip in the transfer characteristics of graphene-based field-effect transistors. *Nanotechnology* **2011**, *22*, 275702.
(8) Di Bartolomeo, A.; Santandrea, S.; Giubileo, F.; Romeo, F.; Petrosino, M.; Citro, R.; Barbara, P.; Lupina, G.; Schröder, T.; Rubino, A. Effect of back-gate on contact resistance and on channel conductance in graphene-based field-effect transistors. *Diamond Relat. Mater.* **2013**, *38*, 19−23.
(9) Avsar, A.; Ochoa, H.; Guinea, F.; Özyilmaz, B.; Van Wees, B.; Vera-Marun, I. J. Colloquium: Spintronics in graphene and other two-dimensional materials. *Rev. Mod. Phys.* **2020**, *92*, 021003.
(10) Hawkes, P. W.; Kasper, E. Principles of Electron Optics. In *Fundamental Wave Optics*; Academic Press, 2022; Vol. 3.
(11) Zhao, Y.; Leuch, A.; Zilberberg, O.; Štrkalj, A. Electron optics using negative refraction in two-dimensional inverted-band *pn* junctions. *Phys. Rev. B* **2023**, *108*, 195301.
(12) Bolotin, K. I.; Ghahari, F.; Shulman, M. D.; Stormer, H. L.; Kim, P. Observation of the fractional quantum Hall effect in graphene. *Nature* **2009**, *462*, 196−199.
(13) Wang, L.; Meric, I.; Huang, P.; Gao, Q.; Gao, Y.; Tran, H.; Taniguchi, T.; Watanabe, K.; Campos, L.; Muller, D.; et al. One-Dimensional Electrical Contact to a Two-Dimensional Material. *Science* **2013**, *342*, 614−617.
(14) Zibrov, A. A.; Kometter, C.; Zhou, H.; Spanton, E.; Taniguchi, T.; Watanabe, K.; Zaletel, M.; Young, A. Tunable interacting composite fermion phases in a half-filled bilayer-graphene Landau level. *Nature* **2017**, *549*, 360−364.
(15) Rhodes, D.; Chae, S. H.; Ribeiro-Palau, R.; Hone, J. Disorder in van der Waals heterostructures of 2D materials. *Nat. Mater.* **2019**, *18*, 541−549.
(16) Son, J.; Kwon, J.; Kim, S.; Lv, Y.; Yu, J.; Lee, J.-Y.; Ryu, H.; Watanabe, K.; Taniguchi, T.; Garrido-Menacho, R.; et al. Atomically precise graphene etch stops for three dimensional integrated systems from two dimensional material heterostructures. *Nat. Commun.* **2018**, *9*, 3988.
(17) Kretz, B.; Pedersen, C. S.; Stradi, D.; Brandbyge, M.; Garcia-Lekue, A. Atomistic insight into the formation of metal-graphene one-dimensional contacts. *Phys. Rev. Appl.* **2018**, *10*, 024016.
(18) Jessen, B. S.; Gammelgaard, L.; Thomsen, M. R.; Mackenzie, D. M.; Thomsen, J. D.; Caridad, J. M.; Duegaard, E.; Watanabe, K.; Taniguchi, T.; Booth, T. J.; et al. Lithographic band structure engineering of graphene. *Nat. Nanotechnol.* **2019**, *14*, 340−346.
(19) Chiu, H.-Y.; Perebeinos, V.; Lin, Y.-M.; Avouris, P. Controllable p-n Junction Formation in Monolayer Graphene Using Electrostatic Substrate Engineering. *Nano Lett.* **2010**, *10*, 4634−4639.
(20) Cheianov, V. V.; Fal'ko, V. I. Selective transmission of Dirac electrons and ballistic magnetoresistance of n - p junctions in graphene. *Phys. Rev. B* **2006**, *74*, 041403.
(21) Hunt, B.; Sanchez-Yamagishi, J. D.; Young, A. F.; Yankowitz, M.; LeRoy, B. J.; Watanabe, K.; Taniguchi, T.; Moon, P.; Koshino, M.; Jarillo-Herrero, P.; Ashoori, R. C. Massive Dirac Fermions and Hofstadter Butterfly in a van der Waals Heterostructure. *Science* **2013**, *340*, 1427−1430.
(22) Wolf, T. M. R.; Zilberberg, O.; Levkivskyi, I.; Blatter, G. Substrate-induced topological minibands in graphene. *Phys. Rev. B* **2018**, *98*, 125408.
(23) Song, S. M.; Park, J. K.; Sul, O. J.; Cho, B. J. Determination of Work Function of Graphene under a Metal Electrode and Its Role in Contact Resistance. *Nano Lett.* **2012**, *12*, 3887−3892.
(24) Shytov, A. V.; Rudner, M. S.; Levitov, L. S. Klein Backscattering and Fabry-Perot Interference in Graphene Heterojunctions. *Phys. Rev. Lett.* **2008**, *101*, 156804.
(25) Yu, Y.-J.; Zhao, Y.; Ryu, S.; Brus, L. E.; Kim, K. S.; Kim, P. Tuning the Graphene Work Function by Electric Field Effect. *Nano Lett.* **2009**, *9*, 3430−3434.
(26) Shi, Y.; Kim, K. K.; Reina, A.; Hofmann, M.; Li, L.-J.; Kong, J. Work Function Engineering of Graphene Electrode via Chemical Doping. *ACS Nano* **2010**, *4*, 2689−2694.
(27) Ziegler, D.; Gava, P.; Güttinger, J.; Molitor, F.; Wirtz, L.; Lazzeri, M.; Saitta, A. M.; Stemmer, A.; Mauri, F.; Stampfer, C. Variations in the work function of doped single- and few-layer graphene assessed by Kelvin probe force microscopy and density functional theory. *Phys. Rev. B* **2011**, *83*, 235434.
(28) Mueller, T.; Xia, F.; Freitag, M.; Tsang, J.; Avouris, P. Role of contacts in graphene transistors: A scanning photocurrent study. *Phys. Rev. B* **2009**, *79*, 245430.
(29) Cusati, T.; Fiori, G.; Gahoi, A.; Passi, V.; Lemme, M. C.; Fortunelli, A.; Iannaccone, G. Electrical properties of graphene-metal contacts. *Sci. Rep.* **2017**, *7*, 5109.
(30) Gutiérrez, C.; Walkup, D.; Ghahari, F.; Lewandowski, C.; Rodriguez-Nieva, J. F.; Watanabe, K.; Taniguchi, T.; Levitov, L. S.; Zhitenev, N. B.; Stroscio, J. A. Interaction-driven quantum Hall wedding cake−like structures in graphene quantum dots. *Science* **2018**, *361*, 789−794.
(31) Chen, H.-Y.; Apalkov, V.; Chakraborty, T. Fock-Darwin States of Dirac Electrons in Graphene-Based Artificial Atoms. *Phys. Rev. Lett.* **2007**, *98*, 186803.
(32) Gu, N.; Rudner, M.; Young, A.; Kim, P.; Levitov, L. Collapse of Landau Levels in Gated Graphene Structures. *Phys. Rev. Lett.* **2011**, *106*, 066601.
(33) Hasan, M. Z.; Kane, C. L. Colloquium: Topological Insulators. *Rev. Mod. Phys.* **2010**, *82*, 3045.
(34) Hatsugai, Y. Chern number and edge states in the integer quantum Hall effect. *Phys. Rev. Lett.* **1993**, *71*, 3697−3700.
(35) Jessen, B. S.; Whelan, P. R.; Mackenzie, D.; Luo, B.; Thomsen, J. D.; Gammelgaard, L.; Booth, T. J.; Bøggild, P. Quantitative optical mapping of two-dimensional materials. *Sci. Rep.* **2018**, *8*, 6381.
(36) Pizzocchero, F.; Gammelgaard, L.; Jessen, B. S.; Caridad, J. M.; Wang, L.; Hone, J.; Bøggild, P.; Booth, T. J. The hot pick-up technique for batch assembly of van der Waals heterostructures. *Nat. Commun.* **2016**, *7*, 11894.
(37) Purdie, D. G.; Pugno, N. M.; Taniguchi, T.; Watanabe, K.; Ferrari, A. C.; Lombardo, A. Cleaning interfaces in layered materials heterostructures. *Nat. Commun.* **2018**, *9*, 5387.
(38) Zalipaev, V. V.; Maksimov, D. N.; Linton, C. M.; Kusmartsev, F. V. Spectrum of localized states in graphene quantum dots and wires. *Phys. Lett. A* **2013**, *377*, 216−221.

https://doi.org/10.1021/acsnano.4c16191
ACS Nano 2025, 19, 18156−18163